

Chapter 3

Characterization of structural and 2DEG transport properties in MOVPE-grown AlGa_N/Ga_N HEMT structures

3.1. Introduction

AlGa_N/Ga_N heterostructures have been attracting much attention as material for realizing high-power and high-frequency electronic devices due to their superior material features, as presented in Chapter 1. A large conduction-band discontinuity and strong piezoelectric effects in AlGa_N/Ga_N heterointerface result in much higher 2DEG densities than those in similar AlGaAs/GaAs heterostructures. In Chapter 2, I presented that AlGa_N/Ga_N heterostructures were successfully grown even on large-area substrates of 100 mm in diameter by MOVPE, and confirmed that the 2DEG density clearly increases with increasing the Al content in AlGa_N layers, in the same manner with the previous theoretical and experimental reports [1-6]. High-Al-content AlGa_N/Ga_N heterostructures seems to be appropriate for realizing high-power-density HEMTs [7,8]. Although the compositional dependence of the 2DEG density has been theoretically discussed [1-3], for the compositional dependence of electron transport properties of AlGa_N/Ga_N heterostructures, there has been no reported systematic study with theoretical discussions, to our knowledge. In order to examine the possibility of AlGa_N/Ga_N HEMTs and to achieve higher device performance, it is essential to understand the correlation between their basic structural and electron transport properties in detail. In this chapter, structural characteristics for different-Al-content AlGa_N/Ga_N heterostructures, such as alloy composition, layer thickness, tensile strain, in-plane stress, crystal quality and bandgap

energy, were investigated in detail by using nondestructive X-ray diffraction measurements and spectroscopic ellipsometry for samples grown on 100-mm-diameter sapphire substrates by MOVPE. Electron transport properties in different-Al-content AlGa_N/Ga_N heterostructures were also theoretically as well as experimentally studied taking into account the structural characterization results.

3.2. Experiment

AlGa_N/Ga_N heterostructures were grown on 100-mm-diameter and 630- μ m-thick *c*-face sapphire substrates using a horizontal MOVPE system (Taiyo Nippon Sanso, SR-4000) with conventional precursors such as trimethylgallium (TMG), trimethylaluminum (TMA), ammonia (NH₃) and monosilane (SiH₄). Substrates were first treated in H₂ flow at 1180°C, and the temperature was then reduced to 500°C for the growth of Ga_N low-temperature buffer layers (LT-BLs). Subsequently, Ga_N and AlGa_N layers were grown at approximately 1100°C. AlGa_N/Ga_N heterostructures consist of, from top to bottom, a 3-nm-thick nondoped AlGa_N layer, a 15-nm-thick silicon-doped AlGa_N layer with a doping density of approximately $5 \times 10^{18}/\text{cm}^3$, a 7-nm-thick nondoped AlGa_N layer, and a 3- μ m-thick Ga_N layer on a 25-nm-thick Ga_N LT-BL. AlGa_N layers were grown at various TMA/TMG input gas ratios to grow different-Al-content AlGa_N/Ga_N layers. The details of growth conditions for AlGa_N layers are described in Chapter 2. The thickness of AlGa_N layers was estimated from the growth rate and confirmed by spectroscopic ellipsometry (J. A. Woollam, VASE®). X-ray diffraction (XRD) measurements were carried out using a Phillips MRD system with a Ge (220) monochromator, in which the Cu K α_1 line ($\lambda = 0.154060$ nm) was used as radiation source operated at 45 kV and 40 mA. The surface morphology was analyzed using atomic force microscopy (AFM) (SPA300, Seiko Instruments Inc.). Hall effect measurements were performed using the van der Pauw technique.

3.3. Results and discussion

3.3.1. XRD and AFM study on strained AlGa_xN layers in different-Al-content AlGa_xN/GaN HEMT structures

When a thin AlGa_xN layer is grown on a thick GaN layer, the AlGa_xN layer is coherently grown on the underlying GaN layer and is strained in the direction of the in-plane tensile [9]. In this case, strained AlGa_xN lattice parameters, instead of intrinsic AlGa_xN lattice parameters, should be taken into account in the determination of the precise alloy composition. To determine the precise alloy composition, lattice constants of strained AlGa_xN layers were measured by XRD 2 θ -scanning for symmetrical (0002) reflections and asymmetric (10-12) reflections. Measured lattice constants are plotted in Figure 3.1 as functions of TMA/(TMA+TMG) input gas ratios. As seen in Figure 3.1, it is clear that the in-plane lattice constant a of AlGa_xN layers is in agreement with that of GaN layers ($x = 0$ in Figure 3.1). This result directly indicates that AlGa_xN layers are coherently strained on the underlying GaN layers.

Al contents x in Al _{x} Ga _{$1-x$} N were calculated according to the equation given by Ref. 9-11. The analytical expressions are as below. For the in-plane biaxial strain, we have:

$$\varepsilon_{xx} = \frac{a - a_0}{a_0}, \quad (3.1)$$

$$\varepsilon_{zz} = \frac{c - c_0}{c_0}, \quad (3.2)$$

$$\varepsilon_{zz} = -2 \frac{C_{11}}{C_{33}} \varepsilon_{xx}, \quad (3.3)$$

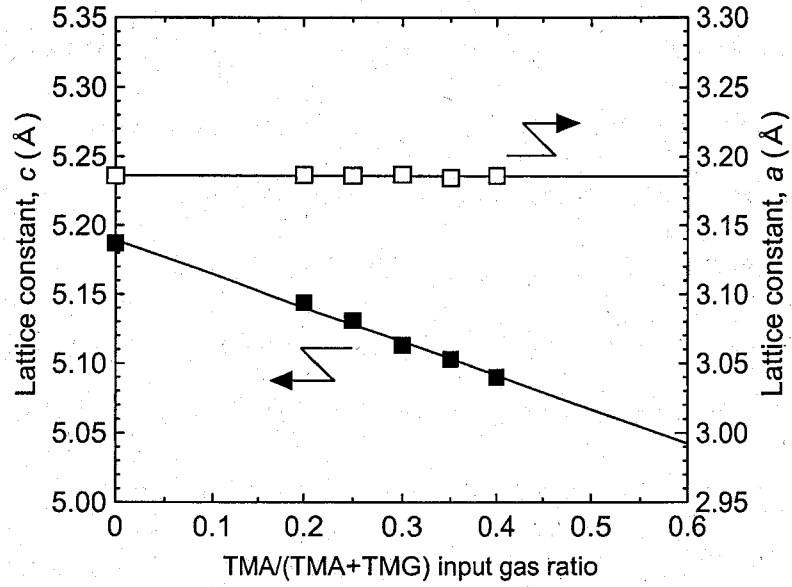


FIG. 3.1. Measured lattice constants of AlGaIn layers on GaN layers grown at various TMA/(TMA + TMG) input gas ratio by MOVPE.

TABLE 3.1. Lattice constants and elastic stiffness constants of GaN and AlN.

	GaN	AlN
a_0 (Å)	3.189 ¹²⁾	3.112 ¹³⁾
c_0 (Å)	5.185 ¹²⁾	4.982 ¹³⁾
$2C_{11}/C_{33}$	0.509 ¹⁴⁾	0.579 ¹⁴⁾
\hat{C} (GPa)	450 ¹⁴⁾	470 ¹⁴⁾

where a_0 and c_0 are the a -axis and c -axis lattice constants of the free-standing AlGa $_x$ N layer, a and c are the a -axis and c -axis lattice constants of the strained AlGa $_x$ N layer, and C_{13} and C_{33} are the elastic stiffness constants of AlGa $_x$ N layers. In this formula, a and c are the measured values. The elastic stiffness constants and the free-standing lattice constants were obtained by assuming a linear relationship between the respective values of GaN and AlN given in Table 3.1 [12-14]. Calculated alloy compositions are plotted in Figure 3.2, as functions of TMA/(TMA+TMG) input gas ratios. As seen in Figure 3.2, a linear relationship is observed between the solid phase and vapor phase composition. Correspondingly, it was confirmed that the coherent Al $_x$ Ga $_{1-x}$ N layers can be grown up to at least $x = 0.42$.

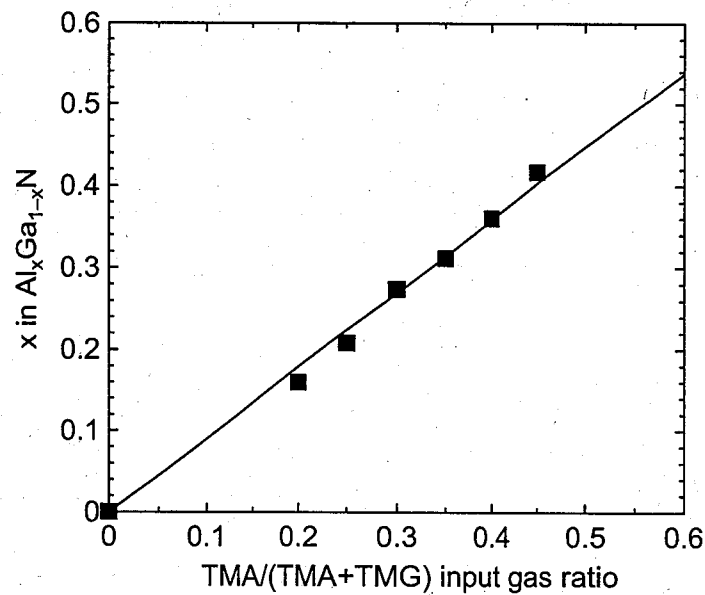


FIG. 3.2. Al contents in AlGa $_x$ N layers on GaN layers grown at various TMA/(TMA + TMG) input gas ratio by MOVPE.

The in-plane stress (σ_{xx}) in AlGa_N layers were also estimated using elastic stiffness constants, according to the calculation given in Ref. 11. The analytical expressions are as below. For the in-plane biaxial stress, we have:

$$\sigma_{xx} = \hat{C}\epsilon_{xx} \quad \text{with} \quad \hat{C} = C_{11} + C_{12} - 2\frac{C_{13}^2}{C_{33}}. \quad (3.4)$$

The elastic stiffness constants were obtained by assuming a linear relation between the respective values of GaN and AlN given from Table 3.1. The calculated results for the tensile strain along the a -axis (ϵ_{xx}) and c -axis (ϵ_{zz}) directions and the in-plane stress (σ_{xx}) for different-Al-content AlGa_N layers on GaN layers are shown in Figure 3.3. As seen in Figure 3.3, the strain ϵ_{xx} and ϵ_{zz} in an AlGa_N layer were calculated to be approximately 0.9% and -0.5%, respectively, when the Al content is 0.42, which seems to be reasonable compared with the previously reported results [10]. Correspondingly, the in-plane stress σ_{xx} in the AlGa_N layer with an Al content of 0.42 was calculated to be approximately 4.0 GPa.

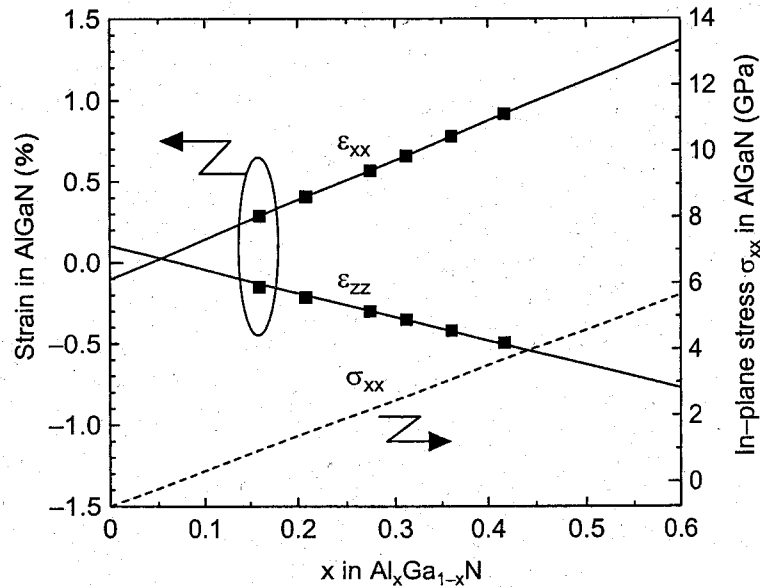


FIG. 3.3. Tensile strain (ϵ_{xx} , ϵ_{zz}) and in-plane stress (σ_{xx}) in MOVPE-grown AlGa_N layers on GaN layers as a function of Al content.

To understand the effects of the tensile strain on the qualities of AlGa_xN layers, crystal and surface qualities were investigated. The crystal quality of AlGa_xN layers was evaluated by XRD ω scanning for AlGa_xN (0002) reflections. Figure 3.4 shows X-ray rocking curve (XRC) full-widths at half maximum (FWHMs) of AlGa_xN (0002) reflections for different-Al-content samples, which represent the tilt distribution of crystals in an AlGa_xN layer. As observed in Figure 3.4, XRC FWHM values were approximately 250 ± 30 arcsec, independent of Al content. This value is almost the same as that of the underlying GaN layers ($x = 0$ in Figure 3.4). Therefore, we can consider that the tilt distribution of AlGa_xN layers is dependent on that of the underlying GaN layers independent of the tensile strain in AlGa_xN layers.

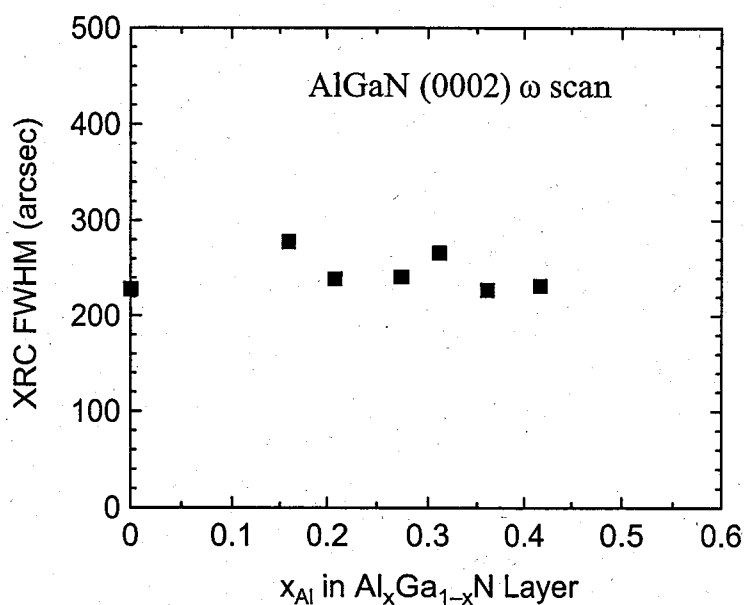


FIG. 3.4. FWHMs of AlGa_xN (0002) X-ray reflection peaks as a function of Al content.

The AFM images of different-Al-content samples are seen in Figure 2.9 in Chapter 2. As observed in Figure 2.9, the surface morphology of AlGa_N/Ga_N heterostructures clearly degrades with increasing Al content. Such morphological features have been observed by several authors and have been attributed either to surface kinetic effects [5], to strain driven three-dimensional growth [15], to partial relaxation [16], or misfit dislocations yield at AlGa_N/Ga_N interfaces [17]. We can also consider that the poor surface morphology of high-Al-content samples is associated with the increased strain in AlGa_N layers.

3.3.2. Spectroscopic ellipsometry study on strained AlGa_N layers in different-Al-content AlGa_N/Ga_N HEMT structures

Spectroscopic ellipsometry was used for the determination not only of layer thickness but also of bandgap energy (E_g) for AlGa_N layers. Ellipsometric measurements determine the phase and amplitude of the complex reflectance ratio $r_p/r_s = \tan(\psi) \cdot e^{i\delta}$, where r_p and r_s are complex field reflectances for *s*- and *p*-polarized lights, respectively, and $\tan(\psi)$ and δ are the standard ellipsometric amplitude and phase parameters. Thus, each ellipsometric measurement yields two parameters, ψ and δ . Figures 3.5(a) and 3.5(b) show the measured ψ and δ of an AlGa_N/Ga_N film grown on a sapphire substrate, respectively, in which Al content has already been estimated to be approximately 0.16 by XRD analysis. In these figures, the peak around 320 nm is related to the exciton of the thin AlGa_N layer. When the wavelength is longer than 370 nm, that is, the photon energy is smaller than the bandgap of Ga_N, interference oscillation in the thick Ga_N layer can be observed. AlGa_N layer thicknesses can be determined by fitting the calculated dielectric functions to the measured results, as seen in Figures 3.5(a) and 3.5(b). From this analysis, the AlGa_N layer thickness was determined to be 25.3 ± 0.3 nm for this sample, which was approximately consistent with that, 24.8 ± 0.1 nm, obtained by cross-sectional transmission electron microscopy (TEM). From this, we can consider that spectroscopic ellipsometry is very useful as a nondestructive and conventional method of

determining the precise AlGaN thickness.

The bandgap energy of AlGaN layers was determined from absorption spectra (see inset in Figure 3.6), which can also be obtained by the ellipsometric measurements and their analysis. We have confirmed that the tensile strain in AlGaN layers is less than 1% for even at Al contents of up to 0.42, as seen in Figure 3.3, so that a change in transition energy due to deformation potential is expected to be small. Figure 3.6 shows the summary of the optical characterization results for strained AlGaN layers. The bowing parameter b for the bandgap of strained AlGaN layers was calculated to be 0.218 eV, which is in good agreement with that (0.25 eV) reported by Takeuchi *et al* [9]. The conduction-band discontinuity (ΔE_C) of the AlGaN/GaN heterointerface was also calculated using the expression $\Delta E_C = 0.75 [E_g(\text{AlGaN}) - E_g(\text{GaN})]$ [18] and plotted in Figure 3.6.

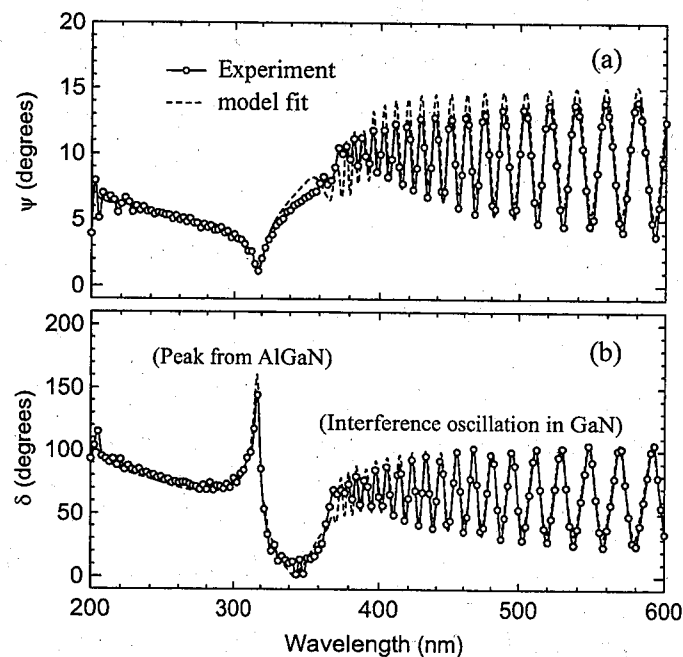


FIG. 3.5. Measured (a) ψ and (b) δ for an MOVPE-grown $\text{Al}_{0.16}\text{Ga}_{0.84}\text{N}/\text{GaN}$ heterostructure on sapphire obtained by spectroscopic ellipsometry at an incidence angle of 75 degrees (solid circles and solid lines, respectively). Calculated ψ and δ (dashed lines) are also shown.

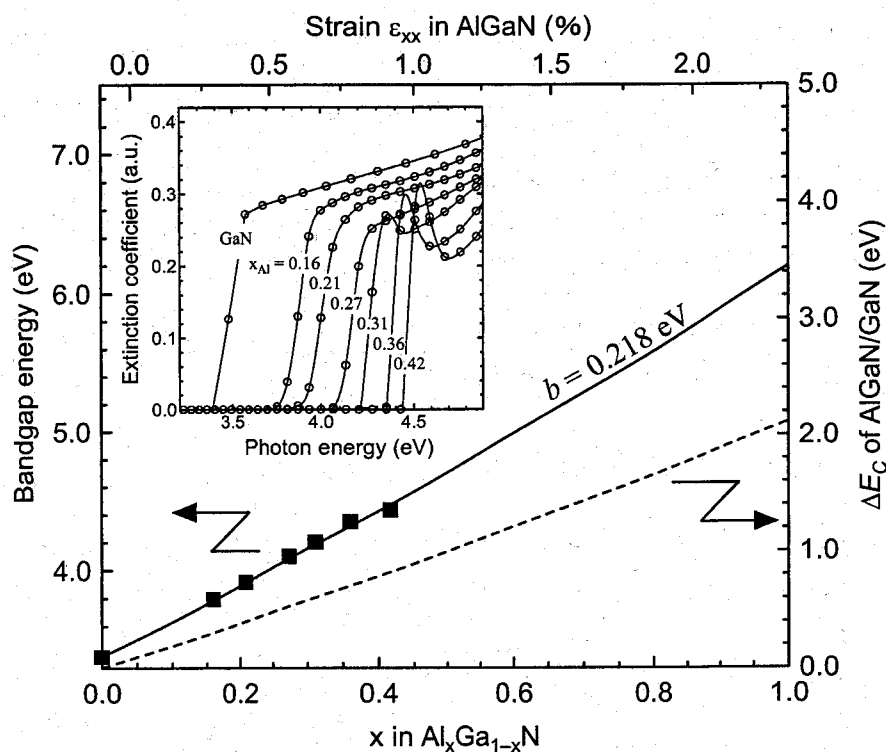


FIG. 3.6. Compositional dependence of bandgap energy in strained AlGaIn layers and of conduction-band discontinuity (ΔE_C) in AlGaIn/GaN heterostructures. Inset shows absorption spectra of different-Al-content AlGaIn layers obtained by spectroscopic ellipsometry.

3.3.3. 2DEG transport properties in different-Al-content AlGaIn/GaN HEMT structures

2DEG density and Hall mobility for different-Al-content AlGaIn/GaN epilayers are seen in Figure 2.12(b) in chapter 2. From this figure, it can be seen that Hall mobility clearly decreases with the increase in Al content. The compositional dependence of 2DEG properties obtained in this study is almost consistent with previously reported results [4-6]. Further investigations are, however, needed to understand the electron transport properties in MOVPE-grown AlGaIn/GaN structures.

To understand the electron transport properties in MOVPE-grown AlGa_{1-x}GaN/GaN structures, we attempted to investigate the carrier scattering mechanism in detail. The scattering theories of 2DEGs in III-V heterostructure system have been well developed by several authors [19-25]. The dominant scattering mechanisms for 2DEGs and bulk III-nitride materials are now well established [26-28] as well as other III-V compounds [29]. In the present calculations of 2DEG mobility in AlGa_{1-x}GaN/GaN structures, we included polar-optical phonons, acoustic phonons, piezoelectric field, alloy disorder, interface roughness and dislocation, mainly according to Ref 26, 27 and 28. We consider the degenerate statistics of 2DEGs for the lowest sub-band occupation for the structure as shown in Figure 3.7.

The analytical expressions for the above-mentioned scattering mechanisms are summarized below for convenience, and material parameters used in the calculation are also listed in Table 3.2 [26].

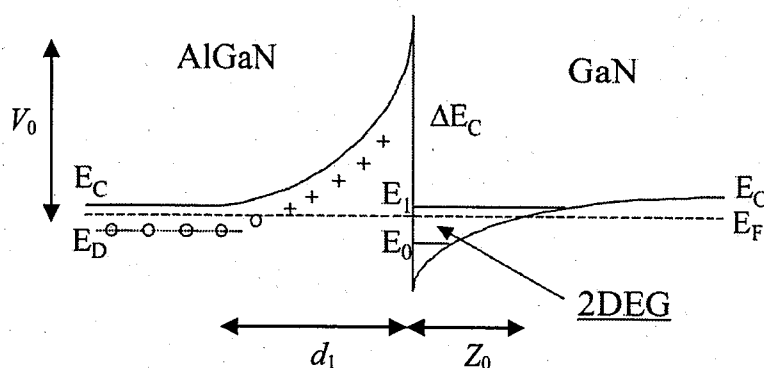


FIG. 3.7. Energy and band diagram of a modulation-doped heterojunction. d_1 is the width of the depletion layer, Z_0 is the average distance of the electronic wave function from heterointerface corresponding to the lowest sub-band.

TABLE 3.2. Material parameters used in the calculations.

Electron effective mass	$m^* = 0.21 m_0$
High frequency dielectric constant	$\epsilon_\infty = 5.35$
Static dielectric constant	$\epsilon_0 = 9.5$
Lattice parameters of Wurtzite GaN	$a_0 = 3.189 \text{ \AA}$ $c_0 = 5.185 \text{ \AA}$
Density of the crystal	$\rho = 6.15 \text{ g/cm}^3$
The width of the quantum well	$Z_0 = 50 \text{ \AA}$
The width of the depletion layer	$d_1 = 3.33 \times 10^{-8} \text{ m}$
LO-phonon energy	$\hbar\omega = 90.5 \text{ meV}$
Longitudinal acoustic phonon velocity	$u_l = 6.56 \times 10^3 \text{ m/s}$
Transverse acoustic phonon velocity	$u_t = 2.68 \times 10^3 \text{ m/s}$
Deformation potential	$E_d = 8.3 \text{ eV}$
Piezoelectric constant	$h_{14} = 0.375 \text{ C/m}^2$
Elastic constants	$c_L = 2.66 \times 10^{11} \text{ N/m}^2$ $c_T = 6.2 \times 10^{10} \text{ N/m}^2$
Impurity density	$N_{BI} = 1 \times 10^{20} / \text{m}^3$
Electron wave vector	$k = 7.3 \times 10^8 \text{ m}^{-1}$
The 2DEG Thomas Fermi wave vector	$q_{TF} = 8.68 \times 10^8 \text{ m}^{-1}$
The effective Bohr radius	$\alpha_B^* = 23.1 \text{ \AA}$

A. Polar-optical-phonon scattering

At high temperatures, the mobility of carriers is limited by the polar-optical-phonon scattering that is comparable to acoustic deformation potential and piezoelectric scattering.

The expression of mobility limited by polar-optical phonon is [22]

$$\mu_{PO} = \frac{4\pi\epsilon_p \hbar^2}{e\omega m^{*2} Z_0} [\exp(\hbar\omega/k_B T) - 1] \epsilon_0, \quad (3.5)$$

where $1/\epsilon_p = 1/\epsilon_\infty - 1/\epsilon_s$, ϵ_∞ and ϵ_s are the dielectric constants of the semiconductor at high and low frequencies, respectively. $\hbar\omega$ is the optical phonon energy, and k_B is the Boltzman constant.

B. Acoustic deformation potential scattering

When the temperature increases, the electron mobility mainly depends on the acoustic-phonon scattering. At most temperatures it is possible to assume that scattering by acoustic phonons is essentially elastic. This assumption is adopted by Ridley [30] and will be used here, as well as the assumption that the phonon population is determined by equipartition. It is assumed that screening is static and that the effects of mechanical and electrical mismatch at the heterojunction can be ignored. The mobility limited by this scattering mechanism is given by [31]

$$\mu_{AC} = \frac{2e\hbar^3 \rho u_l^2 Z_0}{3m^{*3} E_d^2 k_B T_L}, \quad (3.6)$$

where ρ is the density of the crystal, u_l is the longitudinal acoustic phonon velocity, Z_0 and E_d are the effective width of the 2DEG and the deformation potential constant, respectively, as shown in Figure. 3.7 and k_B is the Boltzman constant.

C. Piezoelectric scattering

At intermediate temperatures, the electron mobility is related to piezoelectric scattering in 2DEGs [22]:

$$\mu_{\text{PE}} = \frac{\pi k_{\text{F}} E_{\text{d}}}{Z_0 e h_{14}^2} \frac{1}{\left[\frac{9}{32} + \frac{13}{32} \left(\frac{u_{\ell}}{u_t} \right)^2 \frac{I_{\text{A}}(\gamma_t)}{I_{\text{A}}(\gamma_{\ell})} \right]} \mu_{\text{AC}}. \quad (3.7)$$

Here, h_{14} is piezoelectric constant, u_t is the velocity of transverse acoustic phonon.

$$k_{\text{F}} = (2\pi N_{\text{S}})^{1/2}, \quad (3.8)$$

$$I_{\text{A}}(\gamma_t) = \left[\left(\frac{4\gamma_t}{3\pi} \right)^2 + 1 \right]^{1/2}, \quad (3.9)$$

$$I_{\text{A}}(\gamma_{\ell}) = \left[\left(\frac{4\gamma_{\ell}}{3\pi} \right)^2 + 1 \right]^{1/2}, \quad (3.10)$$

$$\gamma_t = \frac{2\hbar u_t k_{\text{F}}}{k_{\text{B}} T}, \quad (3.11)$$

$$\gamma_{\ell} = \frac{2\hbar u_{\ell} k_{\text{F}}}{k_{\text{B}} T}. \quad (3.12)$$

D. Alloy disorder scattering

Although the wave function that we have used for the 2DEG disappears at the interface, due to the finite potential barrier, some electron density will inevitably penetrate into the AlGaN alloy. Thus it is needed to consider scattering of the electrons due to alloy disorder. Following the procedure outlined in Ref. 21, the relaxation time for alloy disorder scattering is taken to be

$$\frac{1}{\tau_{\text{alloy}}} = \frac{m^* x(1-x)\Omega \langle V \rangle^2}{\hbar^3} \int_{-\infty}^0 |\chi'(z)|^4 dz, \quad (3.13)$$

where $\langle V \rangle$ is the conduction-band offset between AlN and GaN, Ω is the volume of a unit cell, x is the Al fraction in the AlGaIn alloy and $\chi'(z)$ is the part of the wave function which describes the penetration of the electron gas into the alloy:

$$\chi'(z)^2 = \frac{4\pi e^2 N_s}{\epsilon_s V_0} \frac{1}{2} \exp\left[\left(\frac{8m^* V_0}{\hbar^2}\right)^{1/2} z\right]. \quad (3.14)$$

Alloy disorder scattering rates are quite sensitive to the 2DEG density, varying as the square of N_s . This dependence corresponds to the degree to which the electronic wave function penetrates the barrier into the AlGaIn alloy. As alloy disorder is a short-range interaction, the screening of this potential has been neglected.

E. Interface roughness scattering

Interface roughness in layered structures can be in the form of well width fluctuations or alloy fluctuations, both leading to the perturbation of the electron confinement energy [32,33]. The presence of the interface roughness in optical devices can lead to some undesirable effects such as the splitting or broadening of excitonic spectra. The effect is more prominent in narrower wells where few monolayer fluctuations in the well-width result in a large fluctuation in the quantized energy [34]. The carrier transport in quantum wells is mainly limited by interface-roughness scattering [35,36]. Furthermore, at high electric fields, the interface roughness scattering of non-equilibrium LO phonons can render the non-drift hot phonon population, leading to the saturation of the high-field electron drift velocity and inhibition of negative differential resistance (NDR) [37,38]. The influence of interface roughness on the mobility of 2DEDs in AlGaIn/GaN structures is never very precise since the roughness itself is not straightforward to model. Recently, Zanato *et al.* reported the approach assuming that

fluctuations in the interface position are randomly correlated spatially, the correlation being describable by a Gaussian distribution [28]. Regarding the interaction, it was assumed that the variation in the potential that the electron experiences are based on a first-order Taylor expansion of the confining potential [37-39]:

$$\Delta V(\vec{r}) = \frac{e^2 N_s}{2\epsilon_s} \Delta(\vec{r}). \quad (3.15)$$

Taking this as the perturbation and assuming a correlation of the form

$$\langle \Delta V(\vec{r}) \Delta V(\vec{r}') \rangle = \Delta^2 \exp\left[-\frac{|\vec{r} - \vec{r}'|^2}{\Lambda^2}\right], \quad (3.16)$$

where \vec{r} and \vec{r}' are the two-dimensional spatial coordinates, respectively, and Δ and Λ are root mean square (RMS) roughness height and lateral correlation length, respectively. Therefore, the momentum relaxation rate for electrons being scattered from interface roughness is obtained as

$$\frac{1}{\tau_{\text{IFR}}} = \left(\frac{e^2 N_s \Delta \Lambda}{2\epsilon_s}\right)^2 \frac{m^*}{\hbar^3} J(k), \quad (3.17)$$

where

$$J(k) = \int_0^{2k} \frac{\exp(-q^2 \Lambda^2 / 4)}{2k^3 (q + q_s)^2 \sqrt{1 - (q/2k)^2}} q^4 dq. \quad (3.18)$$

Here, $q = 2k \sin(\theta/2)$, θ is the scattering angle and q_s is the screening constant, as [34]

$$q_s = \frac{e^2 m^*}{2\pi\epsilon_s \hbar^2} F(q), \quad (3.19)$$

where $F(q)$ is the form factor defined by [35],

$$F(q) = \int_0^\infty dz \int_0^\infty dz' [f(z)]^2 [f(z')]^2 \exp(-q|z - z'|), \quad (3.20)$$

where $f(z)$ is the Fang-Howard variational wave function [25].

E. Dislocation scattering

The analytical expression for the dislocation scattering rate for a degenerate 2DEG is given by [40,41]

$$\frac{1}{\tau_{\text{dis}}} = N_{\text{dis}} \left(\frac{m^*}{2\pi\hbar^3 \ell_F^3} \right) \int_0^{2k_F} |A(q)|^2 \frac{q^2 dq}{\sqrt{1 - (q/2k_F)^2}}, \quad (3.21)$$

where $k_F = \sqrt{2\pi N_s}$ is the Fermi wave vector, which depends on the 2DEG carrier concentration N_s , N_{dis} is the density of line dislocations, and the screened potential $A(q)$ is given as

$$A(q) = \frac{e}{2\epsilon_s} \frac{2\rho_L}{q(q + q_{\text{TF}})}, \quad (3.22)$$

where ϵ_s is the dielectric constant in the material, the line charge density ρ_L is given to a very good approximation [42,43] by ef/c_0 , where c_0 is the lattice constant in the (0001) direction of wurtzite GaN and f is the fraction of filled state [44]. We have assumed $f = 1$, i.e. that all the acceptor states in the dislocation are filled. Thus the calculated mobility is for the worst case. Here, $q_{\text{TF}} = 2/a^*B$ is the two-dimensional Thomas-Fermi wave vector, a^*B being the effective Bohr radius in the material. Using equations (3.21) and (3.22) with the substitution $u = q/2k_F$, we get the scattering rate as

$$\frac{1}{\tau_{\text{dis}}^{2D}} = \frac{N_{\text{dis}} m^* e^2 \rho_L^2}{\hbar^3 \epsilon_0^2 \epsilon_b^2} \left(\frac{1}{16\pi k_F^4} \right) \int_0^1 \frac{du}{(u + (q_{\text{TF}}/2k_F))^2 \sqrt{1 - u^2}}$$

$$= \frac{N_{\text{dis}} m^* e^2 \rho_L^2}{\hbar^3 \epsilon_0^2 \epsilon_b^2} \frac{I\left(\frac{q_{\text{TF}}}{2k_{\text{F}}}\right)}{16\pi k_{\text{F}}^4}, \quad (3.23)$$

The dimensionless integral $I\left(\frac{q_{\text{TF}}}{2k_{\text{F}}}\right)$ can be evaluated exactly.

F. Comparison between theory and experiment results

To understand the electron transport properties in different-Al-content AlGa_xN/GaN heterostructures, the carrier scattering mechanism was investigated in detail. Various scattering processes, as described above, were taken into account. Calculations were performed using the parameters shown in Figures 2.12(b) and 3.6 (N_{S} : 2DEG density, x_{Al} : Al content, E_{g} : bandgap energy and ΔE_{C} : conduction-band discontinuity). The measured dislocation density in GaN layers ($3 \times 10^9/\text{cm}^2$) was adopted for the calculation of dislocation scattering. The interface roughness scattering was characterized by fitting calculated mobilities to measured results using the parameters of Δ and Λ as shown in the equation (3.17). Here, the calculation was carried out assuming a constant value of 5.0 nm for Λ to focus on interface roughness height. The other parameters are the same as those given in Table. 3.2. The mobilities are combined according to the expression $1/\mu_{\text{total}} = \sum (1/\mu_i)$, where μ_i represents an individual mobility. The calculated mobilities for different-Al-content samples are shown in Figure 3.8 with our experimental results. From Figure 3.8, it is clear that interface roughness has a strong impact on low-temperature 2DEG mobility and has become a predominant scattering process in high-Al-content samples in particular. Figure 3.8 also shows that mobility related to dislocation scattering largely increases with Al content. This is because dislocation scattering sensitively increases with the Fermi wave vector, $k_{\text{F}} = \sqrt{2\pi N_{\text{S}}}$, where N_{S} is 2DEG density (see the equation (3.23)).

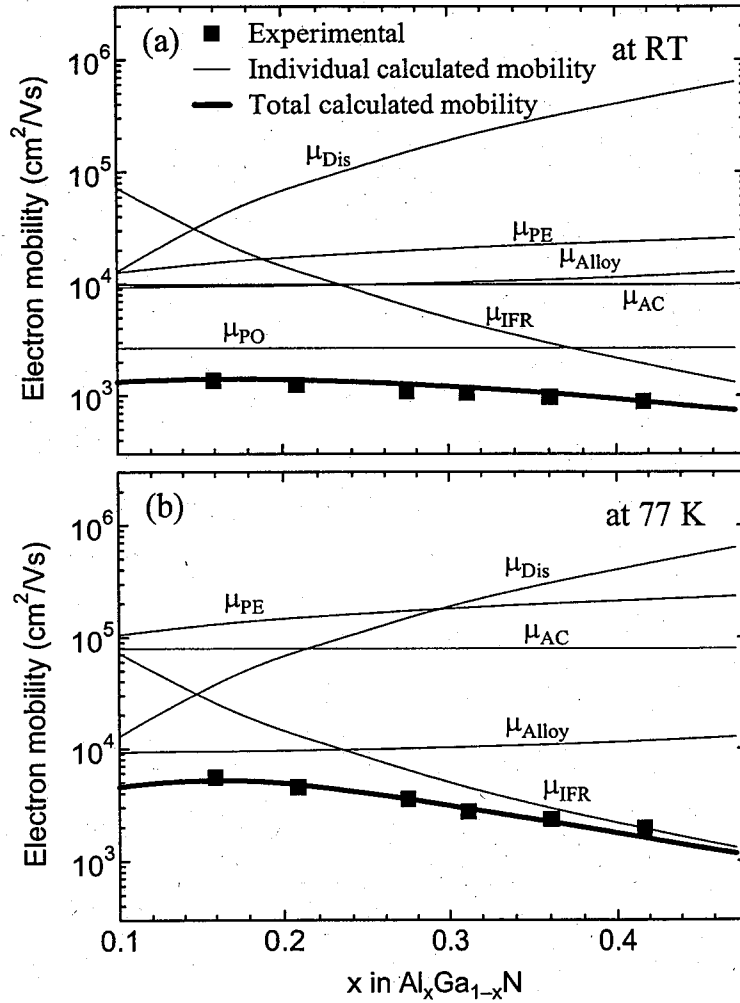


FIG. 3.8. Compositional dependence of Hall mobilities in AlGaN/GaN heterostructures measured at (a) room temperature (RT) and (b) 77 K, and calculated 2DEG mobilities (solid lines) for polar-optical phonons (μ_{PO}), acoustic phonons (μ_{AC}), piezoelectric field (μ_{PE}), interface roughness (μ_{IFR}), dislocation (μ_{Dis}) and alloy disorder (μ_{Alloy}). The total calculated mobilities represent the combined values including all scattering processes according to Matthiessen's rule.

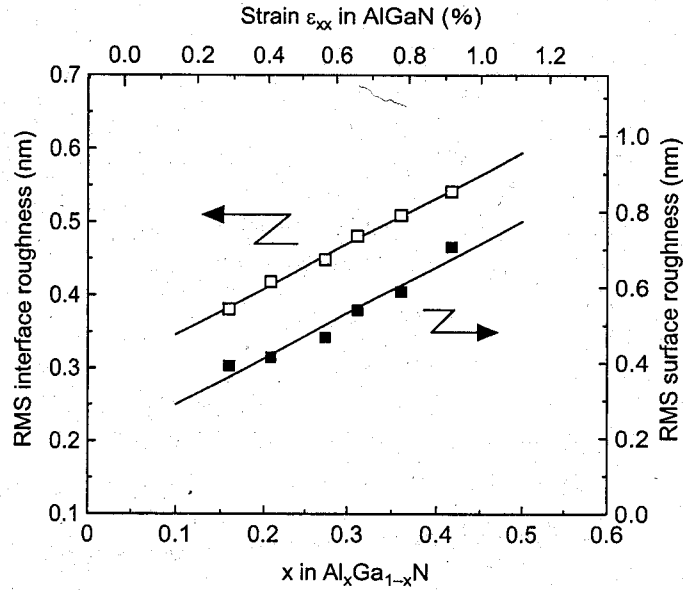


FIG. 3.9. Compositional dependence of calculated RMS interface roughness (RMS Δ) and measured RMS surface roughness of AlGaIn layers.

Figure 3.9 shows the calculated RMS Δ as a function of Al content. As seen in this figure, RMS Δ linearly increases with Al content. From this, it is concluded that lower 2DEG mobilities in higher-Al-content samples originate from the poor interface quality at the AlGaIn and GaN layers. We consider that interface roughness is strongly related to the surface roughness of AlGaIn layers. This is because the interface and surface roughness seems to be related to the structural fluctuation, including misfit dislocations, around the AlGaIn/GaN heterointerface. We have already confirmed, from AFM study, that the surface of MOVPE-grown AlGaIn/GaN films clearly degrades with the increase in Al content, and we discussed that such morphological changes are associated with the increased strain in AlGaIn layers. The RMS surface roughness of AlGaIn layers measured by AFM is also shown in Figure 3.9. As seen in Figure 3.9, it is clear that the dependence of RMS surface roughness on Al content is consistent with the compositional dependence of RMS Δ . Therefore, we can

conclude that the lower mobilities for higher-Al-content samples are attributed to the interface and/or surface roughness. In addition, it can be considered that the degradation of the surface and/or interface is related to strain-induced fluctuations at the AlGa_N/Ga_N heterointerface, including structural and compositional fluctuations induced due to three-dimensional growth or partial relaxation. It should be understood that the tensile strain in AlGa_N layers is affected not only by coherent growth but also by thermal expansion and/or thickness of AlGa_N layers. Therefore, the surface or interface qualities of AlGa_N layers can be modified by changing the growth conditions or film thickness. We believe that the realization of a high-quality surface or interface for higher-Al-content samples could provide higher electron mobilities with a large 2DEG density.

3.4. Conclusion

Different-Al-content AlGa_N/Ga_N heterostructures were grown on 100-mm-diameter sapphire substrates by MOVPE. Their alloy composition, layer thickness, tensile strain, in-plane stress, crystal quality and bandgap energy were determined in detail. The 2DEG properties of those samples were theoretically as well as experimentally investigated taking into account the structural characterization results. It was confirmed that 2DEG density linearly increases with Al content and that low-temperature 2DEG mobility largely decreases with increasing Al content. The theoretical calculation demonstrated that lower 2DEG mobilities in higher-Al-content samples are due to the poor interface quality at the AlGa_N and Ga_N layers. This result is consistent with the experimental result that the surface of MOVPE-grown samples exhibited poor qualities with increasing Al content. It can be considered that the degradation of the surface and/or interface is associated with the increased strain in AlGa_N layers.

References

- [1] F. Bernardini and V. Fiorentini, *Phys. Rev. B* **56**, R10024 (1997).
- [2] Y. Zhang, I. P. Smorchkova, C. R. Elsass, S. Keller, J. P. Ibbetson, S. DenBaars, U. K. Mishra, and J. Singh, *J. Appl. Phys.* **87**, 7981 (2000).
- [3] N. Maeda, T. Nishida, N. Kobayashi, and M. Tomizawa, *Appl. Phys. Lett.* **73**, 1856 (1998).
- [4] I.P. Smorchkova, C. R. Elsass, J. P. Ibbetson, R. Vetury, B. Heying, P. Fini, E. Haus, S. P. Denbaars, J. S. Speck, and U. K. Mishra, *J. Appl. Phys.* **86**, 4520 (1999).
- [5] P. M. Asbeck, E. T. Yu, S. S. Lau, G. J. Sullivan, J. Van Hove and J. Redwing, *Electron. Lett.* **33**, 1230 (1997).
- [6] S. Keller, G. Parish, P. T. Fini, S. Heikman, C.-H. Chen, N. Zhang, S. P. DenBaars, U. K. Mishra, and Y.-F. Wu, *J. Appl. Phys.* **86**, 5850 (1999).
- [7] U. K. Mishra and Y. -F. Wu, *IEEE Trans. Microwave Theory Tech.* **46**, 756 (1998).
- [8] Y.-F. Wu, J. P. Ibbetson, P. Parikh, B. P. Keller, U. K. Mishra and D. Kapolnek, *IEEE Trans Electron Devices* **48**, 586 (2001).
- [9] T. Takeuchi, H. Takeuchi, S. Sota, H. Sakai, H. Amano and I. Akasaki, *Jpn. J. Appl. Phys.* **36**, L177 (1997).
- [10] O. Ambacher, J. Smart, J. R. Shealy, N. G. Weimann, K. Chu, M. Murphy, W. J. Schaff, L. F. Eastman, R. Dimitrov, L. Wittmer, and M. Stutzmann, W. Rieger, and J. Hilsenbeck, *J. Appl. Phys.* **85**, 3222 (1999).
- [11] G. Steude, B. K. Meyer, A. Göldner¹, A. Hoffmann¹, A. Kaschner, F. Bechstedt, H. Amano, and I. Akasaki, *Jpn. J. Appl. Phys.* **38**, L498 (1999).
- [12] W. Yim, E. Stofko, P. Zanzucchi, J. Pankove, M. Ettenberg, and S. Gilbert, *J. Appl. Phys.*, **44**, 292 (1973).

- [13] T. Detchprohm, K. Hiramatsu, K. Itoh, and I. Akasaki, *Jpn. J. Appl. Phys.*, **31**, L1454 (1992).
- [14] A. F. Wright, *J. Appl. Phys.* **82**, 2833 (1997).
- [15] M. Gherasimova, G. Cui, Z. Ren, J. Su, X. L. Wang, J. Han, K. Higashimine, and N. Otsuka, *J. Appl. Phys.* **95**, 2921 (2004).
- [16] Z. Bougrioua, I. Moerman, L. Nistor, B. Van Daele, E. Monroy, E. T. Palacios, F. Calle, and M. Leroux, *Phys. Status Solidi A* **195**, 93 (2003).
- [17] P. Vennéguès, Z. Bougrioua, J. M. Bethoux, M. Azize, and O. Tottereau, *J. Appl. Phys.* **97**, 024912 (2005).
- [18] G. Martin, A. Botchkarev, A. Rockett, and H. Morkoç, *Appl. Phys. Lett.*, **68**, 2541 (1996).
- [19] P. J. Price, *Ann. Phys., NY* **133** 578 (1982).
- [20] K. Lee, M. S. Shur, T. J. Drumond and H. Morkoç, *J. Appl. Phys.* **54**, 6432 (1983).
- [21] W. Walukiewicz, H. E. Ruda, J. Lapowski and H. C. Gatos, *Phys. Rev. B* **30**, 4571 (1984).
- [22] B. K. Ridley, *J. Phys. C: Solid State Phys.* **15**, 5899 (1982).
- [23] E. E. Mendez, P. J. Price and H. Heiblim, *Appl. Phys. Lett.* **45**, 294 (1984).
- [24] K. Hirakawa, H. Sakaki and J. Yoshino, *Appl. Phys. Lett.* **45** 253 (1984).
- [25] F. Stern, *Phys. Rev. B* **5**, 4891 (1972).
- [26] M. Shur, B. Gelmont, and M. A. Khan, *J. Electron. Mater.* **25**, 777 (1996).
- [27] L. Hsu, and W. Walukiewicz, *Phys. Rev. B* **56**, 1520 (1997).
- [28] D. Zanato, S. Gokden, N. Balkan, B. K. Ridley, and W. J. Schaff, *Semicond. Sci. Technol.* **19**, 427 (2004).
- [29] D. L. Rode, *Semiconductors and Semimetals* vol **10**, ed R. K. Willardson and A. C. Beer (New York: Academic) chapter 1 (1975).
- [30] B. K. Ridley, B. E. Foutz and L. F. Eastman, *Phys. Rev. B* **61** 16862 (1999).
- [31] K.V. Arora, A. Naeem, *Phys. Rev. B* **31**, 3887 (1985).

- [32] C. A. Warwick, W. J. Jan and A. Ourmazd, *Appl. Phys. Lett.* **56**, 2666 (1990).
- [33] P. F. Fewster, N. L. Andrew and C. J. Curling, *J. Appl. Cryst.* **21**, 524 (1988).
- [34] B. Deveaud B, J. Y. Emery, A. Chomette, B. Lambert and M. Baudet, *Superlatt. Microstruct.* **3**, 205 (1985).
- [35] K. Hirakawa and H. Sakaki, *Phys. Rev. B* **33**, 8291 (1986).
- [36] R. Gupta and B. K. Ridley, *Phys. Rev. B* **41**, 11972 (1993).
- [37] R. Gupta, N. Balkan and B. K. Ridley, *Semicond. Sci. Technol.* **B 7**, 274 (1992).
- [38] N. Balkan, R. Gupta R, M. E. Daniels, B. K. Ridley and M. Emeny, *Semicond. Sci. Technol.* **5**, 986 (1990).
- [39] H. Sakaki, T. Noda, K. Hirakawa, M. Tanaka and T. Matsusue, *Appl. Phys. Lett.* **51**, 1934 (1987).
- [40] J. Debdeep, A. C. Gossard and U. K. Mishra, *Appl. Phys. Lett.* **76**, 1707 (2000)
- [41] J. H. Davies, *The Physics of Low Dimensional Semiconductor* (Cambridge: Cambridge University Press) (1998).
- [42] D. C. Look and J. R. Sizelove *Phys. Rev. Lett.* **82**, 1237 (1999).
- [43] N. G. Weimann, L. F. Eastman, D. Doppalapudi, H. M. Ng and T. D. Moustakas, *J. Appl. Phys.* **83**, 3656 (1998).
- [44] H. M. Ng, D. Doppalapudi, T. D. Moustakas, N. G. Weiman and L. F. Easrman, *Appl. Phys. Lett.* **73**, 821 (1998).